

The Rewards of Patience: An 822 Day Time Delay in the Gravitational Lens SDSS J1004+4112

J. Fohlmeister¹, C. S. Kochanek², E. E. Falco³, C. W. Morgan^{2,4},
and
J. Wambsganss¹

ABSTRACT

We present 107 new epochs of optical monitoring data for the four brightest images of the gravitational lens SDSS J1004+4112 observed between October 2006 and June 2007. Combining this data with the previously obtained light curves, we determine the time delays between images A, B and C. We confirm our previous measurement finding that A leads B by $\Delta t_{BA} = 40.6 \pm 1.8$ days, and find that image C leads image A by $\Delta \tau_{CA} = 821.6 \pm 2.1$ days. The lower limit on the remaining delay is that image D lags image A by $\Delta \tau_{AD} > 1250$ days. Based on the microlensing of images A and B we estimate that the accretion disk size at a rest wavelength of 2300\AA is $10^{14.8 \pm 0.3}$ cm for a disk inclination of $\cos i = 1/2$, which is consistent with the microlensing disk size-black hole mass correlation function given our estimate of the black hole mass from the MgII line width of $\log M_{BH}/M_{\odot} = 8.44 \pm 0.14$. The long delays allow us to fill in the seasonal gaps and assemble a continuous, densely sampled light curve spanning 5.7 years whose variability implies a structure function with a logarithmic slope of $\gamma = 0.35 \pm 0.02$. As C is the leading image, sharp features in the C light curve can be intensively studied 2.3 years later in the A/B pair, potentially allowing detailed reverberation mapping studies of a quasar at minimal cost.

Subject headings: cosmology: observations – gravitational lensing – quasars: individual: (SDSS J1004+4112)

1. Introduction

The quasar SDSS J1004+4112 at $z_s = 1.734$ is split into five images by an intervening galaxy cluster at $z_l = 0.68$ (Inada et al. 2003; Inada et al. 2005; Oguri et al. 2004). With a maximum image separation of $14''62$, it is a rare example of a quasar gravitationally lensed by a cluster (Wambsganss 2003; Inada et al. 2006). One of the most interesting applications of this system is to use the time delays between the lensed im-

ages to study the structure of the cluster. If we assume the Hubble constant is known, then the delays break the primary model degeneracy of lensing studies (the “mass sheet degeneracy”), and the delay ratios constrain the structure even if the Hubble constant is unknown. After its discovery, several groups modeled the expected time delays in SDSS J1004+4112 and their dependence on the mean mass profile of the cluster (Kawano & Oguri 2006; Oguri et al. 2004; Williams 2004). When we measured the shortest delay in the system, between images A and B, we found a longer delay than predicted by the models (Fohlmeister et al. 2007, hereafter Paper I) where the discrepancy probably arose because the models included the cD galaxy and the cluster halo but neglected the significant perturbations from the member galaxies. As we measure the longer delays, where the cluster potential should

¹Astronomisches Rechen-Institut, Zentrum für Astronomie der Universität Heidelberg, Mönchhofstr. 12-14, 69120 Heidelberg, Germany

²Department of Astronomy, Ohio State University, 140 West 18th Avenue, Columbus, OH 43210

³Smithsonian Astrophysical Observatory, FLWO, P.O. Box 97, Amado, AZ 85645

⁴Department of Physics, United States Naval Academy, 572C Holloway Road, Annapolis, MD 21402

be relatively more important than for the merging A/B image pair, we would not expect cluster substructures to play as important a role.

We also expect this lens to have a fairly short time scale for microlensing variability created by stars either in the intracluster medium or in galaxies near the images. The internal velocities of a cluster are much higher than in a galaxy (700 km/s versus 200 km/s), and SDSS J1004+4112's position on the sky is almost orthogonal to the CMB dipole (Kogut et al. 1993), giving the observer a projected motion on the lens plane of almost 300 km/s. In Paper I, we detected microlensing of the continuum emission of the A/B images in Paper I and there is also evidence for microlensing of the CIV broad line (Richards et al. 2004; Lamer et al. 2006; Gómez-Álvarez et al. 2006). Once we have measured the time delays we can remove the intrinsic quasar variability and use the microlensing variability to estimate the mean stellar mass and stellar surface density, the transverse velocities, and the structure of the quasar source (Gil-Merino et al. 2005; Mortonson et al. 2005; Poindexter et al. 2007; Morgan et al. 2007).

Finally, we note that SDSS J1004+4112 could be an ideal laboratory for studying correlations in the intrinsic variability of quasars. With, image C leading images A and B by 2.3 years, sharp variations in image C can be used to plan intensive monitoring of images A and B to measure the response times as a function of wavelength (e.g. Kaspi et al. 2007), with the additional advantage that the delay between A and B provides redundancies that protect against weather, the Moon and the Sun. The long delays between the images also mean that seasonal gaps are completely filled, and we can examine the structure function of the variability with a densely-sampled, gap-free light curve (modulo corrections for microlensing). Such data generally do not exist, since most time variability data for quasars (other than nearby reverberation mapping targets, e.g. Peterson et al. 2004) have very sparse sampling (e.g. Hawkins 2007 on long time scales for a small number of objects or Vanden Berk et al. 2004 on shorter time scales for many objects).

In Paper I (Fohlmeister et al. 2007) we presented three years of optical monitoring data for the four brightest images of SDSS J1004+4112 spanning 1000 days from December 2003 to June

2006. The fifth quasar image, E, is too faint to be detected in our observations. We measured the time delay between the A and B image pair to be $\Delta\tau_{BA} = 38.4 \pm 2.0$ days. While larger separation lenses tend to have longer time delays, for these two images the propagation time difference is small, because they form a close image pair (3''.8) from the source lying close to a fold caustic. For the more widely separated C and D images we could only estimate lower limits on the delays of 560 and 800 days relative to image B and A. In this paper we present the 107 new optical monitoring epochs for the 2006/2007 season in §2. When combined with our previous data we have light curves spanning 1250 days that allow us to measure the AC delay in §3. In §4 we use the microlensing variability of the A/B images to measure the size of the quasar accretion disk, and in §5 we measure the structure function of the intrinsic variability. We discuss the future prospects for exploiting this system in §6.

2. Data

We monitored SDSS J1004+4112 in the r-band during the 2006-2007 season using the Fred Lawrence Whipple Observatory (FLWO) 1.2m telescope on Mount Hopkins and the MDM 2.4m Hiltner Telescope on Kitt Peak. The FLWO observations were obtained with Keplercam (0''.672 pixels) and the MDM observations with RETROCAM (Morgan et al. 2005) (0''.259 pixels). The data reduction was carried out as described in Paper I. We continued to use the same five stars to set the PSF model and the flux scale of each epoch and verified that these flux standards continue to show no variability. Table 1 presents the photometry for the four images in the 2006-2007 season.

In Figure 1 we present the resulting light curves for images A to D for the period from December 2003 to June 2007. The average sampling rate during the 2006/2007 season is once every third day. The FLWO data are noisy, so for Figure 1 we show a running average of the data (one point every five days averaged over ± 7 days) to emphasize the long term trends. Images C and D are offset by 0.3 and 1.0 mag, respectively, so that they do not overlap with image B in the third and fourth season. During this season, images A and

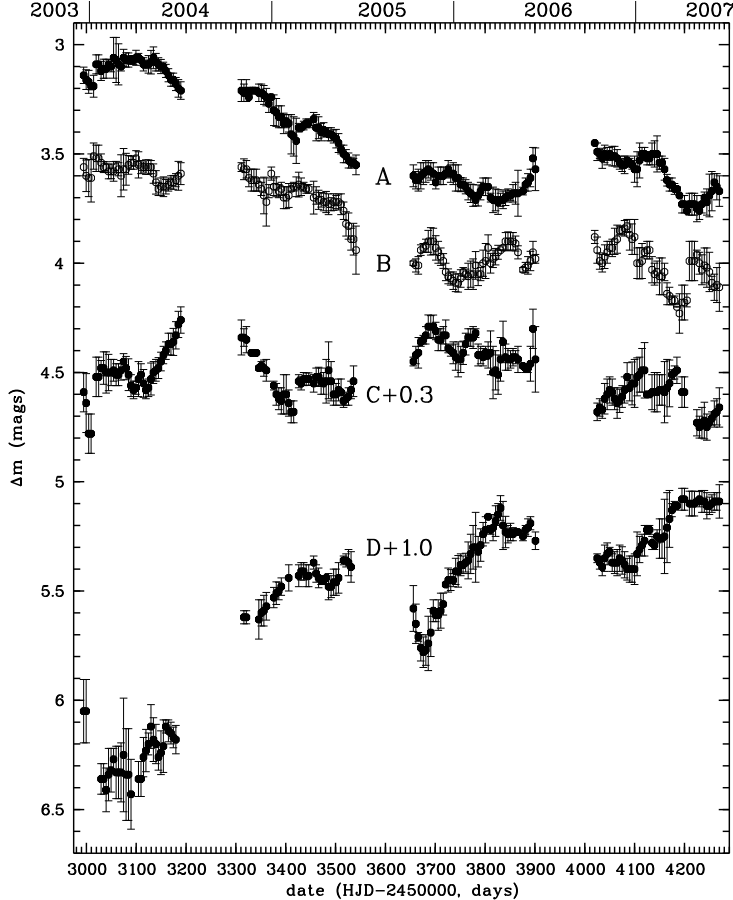


Fig. 1.— Light curves of the A, B, C and D images of the quasar SDSS J1004+4112 from December 2003 to June 2007. Images C and D have been offset by 0.3 and 1.0 mag, respectively, in order to avoid overlap. We present a running average of one point every 5 days averaged over ± 7 days to emphasize trends and to avoid confusion by noise.

B faded by approximately 0.4 mag with a prominent feature near the middle of the season, image C was relatively constant and image D brightened by about 0.4 mag. For the full four seasons, A and B have faded by approximately 1 mag, C has remained relatively constant and D has brightened by about 1.5 mag.

3. The Time Delay

For the determination of the time delay, we use the methods described in Paper I. Our first step with the new data was to remeasure the A/B delay. The fourth season shows a nice feature with maxima in images A and B near

days 4120 and 4080 respectively, followed by a roughly 100 day decline to minima at 4220 (A) and 4180 (B) days. With the dispersion method (Pelt et al. 1994; Pelt et al. 1996) we measure the delay between A and B to be $\Delta t_{BA} = 40.1 \pm 3.5$ days. For the Kochanek et al. (2006) polynomial method we used polynomial orders of $N_{src} = 20, 40, 60$ and 80 for the source and $N_{\mu} = 1, 2, 3$ and 4 for the microlensing variability and derived the final estimate using the Bayesian weighting of these cases described in Poindexter et al. (2007). We found delays of 40.6 ± 1.8 , 40.1 ± 1.8 and 39.8 ± 1.8 (68% confidence regions) depending on whether we weighted the changes in the number of parameters using the Bayesian

information criterion (which strongly penalizes extra parameters), the Akaike information criterion (which weakly penalizes extra parameters) or no penalty for extra parameters. These are consistent with our result from Paper I of $\Delta\tau_{BA} = 38.4 \pm 2.0$ days, but are somewhat more conservative in their treatment of the parameterization and the role of microlensing.

In Paper I we derived a lower limit on the BC delay of $\Delta\tau_{CB} > 560$ days and suggested, based on some similarities between the third season for A/B with the first season for C, that a delay of order 700 days was plausible but statistically too weak to claim as a measurement. We now see that the feature in the second season for image C strongly matches the feature we observe in the new season for A and B. Using the dispersion spectra method (Pelt et al. 1994, 1996), we find $\Delta\tau_{CA} = 822 \pm 7$ days and $\Delta\tau_{CB} = 780 \pm 6$ days where the CA delay is slightly less accurate because the CA overlap is slightly less than the CB overlap due to the alignment of the light curves relative to the seasonal gaps. The three delays are mutually consistent since $\Delta\tau_{CB} = \Delta\tau_{CA} - \Delta\tau_{BA} = 782 \pm 7$ days. For the polynomial method analysis we simultaneously fit A, B and C holding the A/B delay fixed to 40.6 days to find CA delays of 821.6 ± 2.1 , 823.0 ± 2.1 and 820.2 ± 2.1 days for the three weighting methods, respectively. Image D should lag the other three images, and we see no feature in the light curve of image D that can be matched to the first season of images A/B. The lower limit on the time delay between images A and D is now $\Delta\tau_{DA} > 1250$ days (3.4 years).

We modeled the lens using the same approach as in Paper I, where we include the central cD galaxy, and NFW halo for the cluster dark matter and 12 pseudo-Jaffe models corresponding to cluster galaxies (we added an extra component at $(x, y) = (31''.0, 4''.0)$ relative to quasar image A in an effort to reduce the overall shear). The fits were carried out using *lensmodel* (Keeton 2001) and while adequate they are not satisfactory – it is very difficult to find solutions with no additional quasar images created by the galaxies, and checking for the extra images makes the procedure extraordinarily slow. At present we lack the ability to model this system in detail (including uncertainties) at the precision of the constraints, while simplified models that ignore the galaxies are inca-

pable of fitting the data at all. The model predicts an AD delay of order 2000 days (5.5 years), which is consistent with our current lower bound.

4. Microlensing and the Size of the Quasar Accretion Disk

The residuals of the A and B light curves (see Fig. 2) clearly indicate that microlensing is present. After correcting for the time delay, the mean magnitude differences between A and B for the four seasons are 0.460 ± 0.005 , 0.283 ± 0.007 , 0.339 ± 0.005 and 0.381 ± 0.007 mag. For the two seasons overlapping with C we find mean magnitude differences, seasonal gradients and second derivatives of 0.590 ± 0.010 mag, -0.04 ± 0.02 mag/year and 0.29 ± 0.09 mag/year² for C relative to A and 0.368 ± 0.005 mag, 0.05 ± 0.01 mag/year and 0.18 ± 0.04 mag/year² for B relative to A. Fig. 2 shows the superposition of the phased A, B and C light curves and the differences between them that are the signature of microlensing.

We modeled the microlensing for images A/B using the Bayesian Monte Carlo method of Kochanek (2004). We used the microlensing parameters of our (adequate) lens model, with convergence κ and shear γ values of $\kappa = 0.48$ and $\gamma = 0.57$ for A and $\kappa = 0.47$ and $\gamma = 0.39$ for B. We allowed the surface density in stars κ_* to vary from 10% to 100% of κ increments of 10%. We used a microlens mass function with $dn/dM \propto M^{-1.3}$ with a dynamic range in mass of a factor of 50 that approximates the Galactic disk mass function of Gould (2000). We generated 4096×4096 pixel magnification patterns with an outer scale of $20\langle R_E \rangle$ where $\langle R_E \rangle$ is the Einstein radius at the mean stellar mass $\langle M \rangle$. We modeled the disk as a face-on, thin disk (Shakura & Syun'yaev 1973) neglecting the central temperature depression and relativistic effects. We measure the disk size R_λ as the point where the disk temperature matches the rest-frame energy of our monitoring band, $kT_\lambda = hc/\lambda$, where $\lambda \simeq 2300\text{\AA}$ for the r-band at the source redshift (see Morgan et al. 2007). The half-light radius $R_{1/2} = 2.44R_\lambda$ should be used to compare to any other disk model, since Mortonson et al. (2005) have shown that the half-light radius depends little on the surface brightness profile of

the model. We made four realizations of each of the 10 microlensing models and drew 2×10^5 trial light curves for each of the 40 cases so that we would have a reasonable statistical sampling of light curves that fit the data well. We found that

$$R_{2300\text{\AA}} = 10^{14.8 \pm 0.3} \frac{\text{cm}}{h_{70} \sqrt{\cos i}} \quad (1)$$

for a disk inclination angle i , whether or not we use a prior on the mean microlens mass of $0.1 M_\odot < \langle M \rangle < M_\odot$.

From the MgII emission line width/black hole mass calibration of Kollmeier et al. (2006), the spectrum of image C from Richards et al. (2004), and a magnification-corrected HST *I*-band magnitude of 20.9 ± 0.4 , we estimate a black hole mass of $\log M_{BH}/M_\odot = 8.4 \pm 0.2$. Fig. 3 compares the disk size estimate to the characteristic scales of such a black hole.

5. The Structure Function

The quasar structure function can be used as a tool to characterize quasar variability independent of short-timescale monitoring gaps and to compare with theoretical models of quasar variability (e.g. Kawaguchi et al. 1998). The structure function

$$S(\tau) = \sqrt{\frac{1}{N(\tau)} \sum_{i < j} [m(t_j) - m(t_i)]^2} \quad (2)$$

is the variance in the magnitude as a function of the time $\tau = t_j - t_i$ between measurements where $m(t_j)$ and $N(\tau)$ is the number of epochs at that time lag. For SDSS J1004+4112 we can determine the structure function over a moderate time range and with a dense sampling rate and no seasonal gaps if we use the time-delay corrected quasar light curves for images B and C. These cover a time-baseline of 2065 days (5.7 years) in the observers frame, corresponding to a maximum rest-frame time lag at $z_s = 1.734$ of 755 days. For the very different behavior of the image D light curve, which could not yet be time-delay connected to the other images, we compute the structure function independently for rest frame time lags up to 470 days. As in Vanden Berk et al. 2004 we fit the form of the structure function with a power law. The value for the power law index $\gamma = 0.35 \pm 0.02$ for the combined image B and C light curves is consistent with that derived for

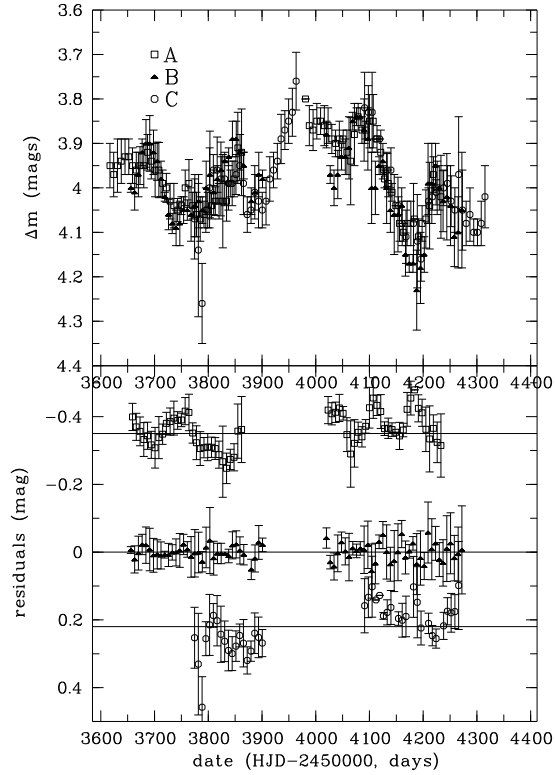


Fig. 2.— The image A, B and C light curves in their overlap region after shifting by the time delays. The data are binned in one week intervals. The lower box shows the residual magnitudes shifted by the offset between the images, revealing microlensing variability of order 0.15 mag. The light curve of image B was chosen to have constant flux because it has the most overlap with the other two.

the SDSS quasar sample. For image D we find a similar slope of $\gamma = 0.39 \pm 0.03$, as expected from the light curve. Time-delay connecting the image A, B and C lightcurves by subtracting the estimated microlensing variability in the overlap region of the lightcurves gives a restframe record of the intrinsic quasar variability over 500 days. The slope of the structure function for the source light curve $\gamma_s = 0.45 \pm 0.03$ is steeper than for the observed non-microlensing corrected curves.

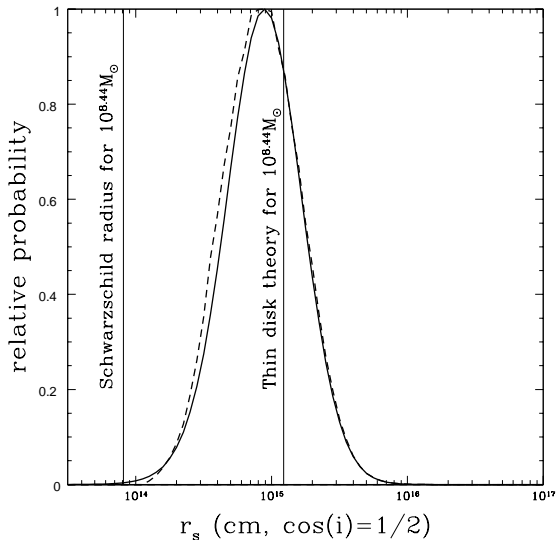


Fig. 3.— Probability distribution for the accretion disk size at 2300\AA assuming the mean disk inclination ($\cos(i) = 1/2$). The solid (dashed) curves show the distribution without (with) the prior on the average microlens mass. The vertical lines show the Schwarzschild radius and the expected size for thin disk theory assuming the black hole mass estimated from the MgII emission line width. The expectation from thin disk theory assumes the disk is radiating at Eddington ($L/L_E = 1$) with efficiency $\eta = 0.1$ where $L = \eta \dot{M} c^2$.

6. Summary and Conclusions

We present a fourth season of monitoring data for the four bright images of the five image gravitational lens system SDSS J1004+4112. We confirm our previous estimate for the time delay between the merging A/B pair, finding that B leads A by 40.6 ± 1.8 days. We measure the delay for image C for the first time, finding that it leads image A by 821.6 ± 2.1 days. We note that this is nearly twice the longest previously measured delay (the 417 day delay in Q0957+561 (Schild & Thomson 1995; Kundic et al. 1997)). We find a lower bound that D lags A by more than approximately 1250 days. Our current mass model predicts that D lags A by approximately 2000 days, which is consistent with the present limit. The fractional uncertainties in the AB delay

are still dominated by sampling and microlensing, while the fractional uncertainties in the AC delay are dominated by cosmic variance due to density fluctuations along the line of sight rather than our measurement uncertainties of 0.3% (e.g. Barkana 1996).

A detailed model of this system, including the constraints from the multiply imaged, higher redshift arcs (Sharon et al. 2005), the X-ray measurements (Ota et al. 2006; Lamer et al. 2006) and a detailed understanding of the uncertainties will be a challenge. We lack a completely satisfactory model for the system at present, in the sense that the modeling process is extraordinarily slow due to the ability of the gravitational potentials associated with the cluster member galaxies to generate additional but undetected images of the quasar, making it impossible to carry out a reliable model survey. The record of models for this system is discouraging. As we noted in Paper I, all three model studies (Oguri et al. 2004; Williams & Saha 2004; Kawano & Oguri 2006) generically predicted shorter AB delays than the observed 40 days, and that this could be plausibly explained by the absence of substructure (i.e. galaxies) in the potential models. The longer AB-C and AB-D delays should be less sensitive to substructure. Oguri et al. (2004) do not include an estimate of the AB-C delays and have A-D delays consistent with our present limits. The range of B-C delays in Williams & Saha (2004) is consistent with our measurement of 820 days, but they predict AD delays shorter than our current lower bound of 1250 days. Kawano & Oguri (2006) predict a range for the longer delays over a broad range of mass distributions, none of which match our delays in detail. However, models with sufficiently long C-B delays generally have C-D delays long enough to agree with our present limits.

Based on our present mass model we used the microlensing between the A and B images to make an estimate of the size of the quasar accretion disk at 2300\AA in the quasar rest frame. If we convert this to the expected size at 2500\AA assuming the $R_\lambda \propto \lambda^{4/3}$ scaling for a thin disk and assume the mean disk inclination $\cos(i) = 1/2$ the scale on which the disk temperature matches the photon energy is $R_{2500\text{\AA}} = 10^{15.0 \pm 0.3}$ cm. Comparisons to other disk models should use the half-light radius which is 2.44 times larger. Based on the quasar

MgII emission line width we estimate that the black hole mass is $10^{8.4 \pm 0.2} M_{\odot}$. For this mass, the microlensing accretion disk size-black hole mass correlation found by Morgan et al. (2007) predicts that $R_{2500\text{\AA}} = 10^{15.3}$ cm, which is in broad agreement with the measurement. Further observations, the inclusion of additional images, and monitoring in multiple bands should improve these measurements and potentially allow us to determine the mean surface density in stars near the images κ_* and their average mass $\langle M \rangle$. Similarly, the ability to construct continuous light curves of the intrinsic variability and to use image C to provide early warning of sharp flux changes that can then be intensively monitored in images A and B may make this system a good candidate for applying reverberation mapping techniques to a massive, luminous quasar. At present, we already see that the system has a structure function typical of quasars.

We thank all the participating observers at both the Harvard-Smithsonian Center for Astrophysics and the MDM Observatory for their support of these observations. This work is also based on observations obtained with the MDM 2.4m Hiltner and 1.3m McGraw-Hill telescopes, which are owned and operated by a consortium consisting of Columbia University, Dartmouth College, the University of Michigan, the Ohio State University and Ohio University. We thank N.F. Bate for valuable comments and encouragements. We also acknowledge support by the European Community's Sixth Framework Marie Curie Research Training Network Programme, Contract No. MRTN-CT-2004-505183 "ANGLES".

REFERENCES

- Barkana, R., 1996, *ApJ*, 468, 17
- Fohlmeister, J. et al. 2007, *ApJ*, 662, 62
- Gil-Merino, R., Wambsganss, J., Goicoechea, L.J., Lewis, G.F. 2005, *A&A*, 432, 83
- Gómez-Álvarez, P., Mediavilla, E., Muñoz, J.A., Arribas, S., Sánchez, S.F., Oscoz, A., Prada, F., & Serra-Ricart, M., 2006, *ApJL*, 645, 5
- Gould, A. 2000, *ApJ*, 535, 928
- Hawkins, M. R. S. 2007, *A&A*, 462, 581
- Inada, N. et al. 2003, *Nature*, 426, 810
- Inada, N. et al. 2005, *PASJ*, 57, L7
- Inada, N. et al. 2006, *ApJ*, 653, 97
- Kaspi, S., Brandt, W.N., Maoz, D., Netzer, H., Schneider, D.P., & Shemmer, O. 2007, *ApJ*, 659, 997
- Kawaguchi, T., Mineshige, S., Umemura, M., & Turner, E.L. 1998, *ApJ*, 504, 671
- Kawano, Y., & Oguri, M. 2006, *PASJ*, 58, 271
- Keeton, C. R. 2001, *astro-ph/0102340*
- Kochanek, C. S. 2004, *ApJ*, 605, 58
- Kochanek, C. S., Schneider, P., Wambsganss, J. 2006, *Gravitational Lensing: Strong, Weak & Micro*, Proceedings of the 33rd Saas-Fe Advanced Course, G. Meylan, P. Jetzer & P. North, eds. (Springer Verlag: Berlin)
- Kochanek, C. S., Morgan, N. D., Falco, E. E., McLeod, B. A., Winn, J. N., Dembicky, J., & Ketzeback, B. 2006, *ApJ*, 640, 47
- Kogut, A., et al., 1993, *ApJ*, 419, 1
- Kollmeier, J. A. et al. 2006, *ApJ*, 648, 128
- Kundic, T., Turner, E.L., Colley, W.N., Gott, J.R., Rhoads, J.E., Wang, Y., Bergeron, L.E., Gloria, K.A., Long, D.C., Malhotra, S., & Wambsganss, J., 1997, *ApJ*, 482, 75
- Lamer, G., Schwoppe, A., Wisotzki, L., Christensen, L., 2006, *A&A*, 454, 493
- Morgan, C.W., Byard, P.L., Depoy, D.L., Derwent, M., Kochanek, C.S., Marshal, J.L., O'Brien, T.P., & Pogge, R.W., 2005, *AJ*, 129, 2504
- Morgan, C.W., Kochanek, C.S., Morgan, N.D., Falco, E.E., 2007, *astro-ph/0707.0305*
- Mortonson, M.J., Schechter, P.L. & Wambsganss, J. 2005, *ApJ*, 628, 594
- Oguri, M., et al. 2004, *ApJ*, 605, 78
- Ota, N., et al. 2006, *ApJ*, 647, 215
- Pelt, J., Hoff, W., Kayser, R., Refsdal, S., & Schramm, T. 1994, *A&A*, 286, 775

- Pelt, J., Kayser, R., Refsdal, S., & Schramm, T.
1996, A&A, 305, 97
- Peterson, B.M., et al. 2004, ApJ, 613, 682
- Poindexter, S., Morgan, N.D., Kochanek, C.S.,
2007, astro-ph/0707.0003
- Richards, G. T., et al. 2004, ApJ, 610, 679
- Schild, R.E., & Thomson, D.J., 1995, Aj, 109,
1070
- Shakura, N. I., Syunyaev, R. A. 1973, A&A, 24,
337
- Sharon, K. et al. 2005, ApJ, 629, 73
- Vanden Berk, D.E., et al., 2004, ApJ, 601, 692
- Wambsganss, J., 2003, Nature, 426, 781
- Williams, L. L. R. & Saha, P. 2004 , AJ, 128, 2631

TABLE 1
LIGHT CURVES FOR SDSS J1004+4112 *

HJD	χ^2/N_{dof}	Image A	Image B	Image C	Image D	Observatory	Detector
4019.006	1.15	3.451±0.027	3.880±0.027	4.332±0.027	4.323±0.027	MDM	RETROCAM
4029.001	1.99	3.488±0.027	3.952±0.027	4.382±0.027	4.347±0.027	MDM	RETROCAM
4031.006	1.46	3.529±0.027	3.985±0.027	4.413±0.027	4.361±0.027	MDM	RETROCAM
4035.026	0.99	3.477±0.027	4.024±0.027	4.326±0.027	4.395±0.027	MDM	RETROCAM
4035.980	2.20	3.511±0.027	3.997±0.027	4.344±0.027	4.362±0.027	MDM	RETROCAM
4039.016	2.02	3.576±0.027	4.061±0.027	4.394±0.027	4.434±0.027	MDM	RETROCAM
4043.955	0.86	3.514±0.027	3.924±0.027	4.249±0.027	4.297±0.027	MDM	RETROCAM
4044.949	0.95	3.525±0.027	3.930±0.027	4.256±0.027	4.318±0.027	MDM	RETROCAM
4045.966	0.77	3.472±0.027	3.985±0.027	4.451±0.040	4.274±0.034	MDM	RETROCAM
4046.966	1.03	3.512±0.027	3.916±0.027	4.271±0.027	4.285±0.027	MDM	RETROCAM
4047.004	0.47	3.427±0.103	3.915±0.158	4.415±0.252	4.625±0.298	FLWO	Keplercam
4048.968	1.34	3.518±0.027	3.924±0.027	4.276±0.027	4.337±0.027	MDM	RETROCAM
4050.008	0.97	3.523±0.027	3.943±0.027	4.245±0.027	4.322±0.027	MDM	RETROCAM
4054.008	0.59	3.486±0.027	3.877±0.034	4.258±0.049	4.344±0.052	FLWO	Keplercam
4059.902	1.41	3.580±0.027	3.998±0.027	4.415±0.027	4.393±0.027	MDM	RETROCAM
4059.947	1.46	3.490±0.027	3.936±0.027	4.291±0.027	4.419±0.027	FLWO	Keplercam
4060.884	2.58	3.477±0.027	3.908±0.027	4.282±0.027	4.412±0.027	FLWO	Keplercam
4065.001	0.92	3.498±0.027	3.875±0.028	4.339±0.042	4.330±0.041	FLWO	Keplercam
4066.006	0.80	3.507±0.048	3.824±0.063	4.313±0.100	4.301±0.098	FLWO	Keplercam
4067.965	1.40	(3.655±0.027)	(4.007±0.027)	4.487±0.027	4.440±0.027	MDM	RETROCAM
4070.954	1.16	3.522±0.027	3.835±0.027	4.330±0.041	4.307±0.040	FLWO	Keplercam
4071.884	0.96	3.566±0.027	3.854±0.027	4.292±0.027	4.306±0.027	MDM	RETROCAM
4072.014	1.48	3.525±0.027	3.858±0.027	4.323±0.027	4.319±0.027	FLWO	Keplercam
4072.890	1.08	3.533±0.046	3.820±0.059	4.317±0.094	4.304±0.092	FLWO	Keplercam
4072.949	0.81	3.554±0.027	3.867±0.027	4.298±0.027	4.385±0.027	MDM	RETROCAM
4073.894	0.61	3.585±0.027	3.865±0.027	4.345±0.035	4.332±0.035	MDM	RETROCAM
4074.897	1.27	3.573±0.027	3.841±0.027	4.285±0.027	4.301±0.027	MDM	RETROCAM
4074.996	1.02	3.509±0.037	3.873±0.051	4.350±0.079	4.390±0.081	FLWO	Keplercam
4075.993	0.86	3.550±0.041	3.797±0.051	4.310±0.081	4.464±0.093	FLWO	Keplercam
4076.029	1.11	3.604±0.027	3.848±0.027	4.349±0.027	4.313±0.027	MDM	RETROCAM
4081.022	1.29	3.550±0.033	3.866±0.043	4.178±0.057	4.436±0.072	FLWO	Keplercam

TABLE 1—*Continued*

HJD	χ^2/N_{dof}	Image A	Image B	Image C	Image D	Observatory	Detector
4082.865	1.23	3.521±0.028	3.802±0.034	4.192±0.049	4.334±0.055	FLWO	Keplercam
4084.972	0.82	3.506±0.027	3.844±0.027	4.280±0.027	4.390±0.027	FLWO	Keplercam
4086.877	0.91	3.524±0.027	3.826±0.034	4.242±0.049	4.424±0.057	FLWO	Keplercam
4092.985	0.62	3.557±0.031	3.944±0.043	4.256±0.057	4.427±0.067	FLWO	Keplercam
4093.956	3.20	3.527±0.027	3.782±0.033	4.250±0.051	4.330±0.054	FLWO	Keplercam
4094.999	0.62	3.539±0.027	3.849±0.035	4.242±0.051	4.451±0.061	FLWO	Keplercam
4096.038	2.08	(3.692±0.027)	3.990±0.027	4.408±0.027	4.454±0.027	MDM	RETROCAM
4096.050	1.25	3.567±0.027	3.870±0.028	4.214±0.038	4.320±0.041	FLWO	Keplercam
4100.947	1.00	3.567±0.033	3.892±0.043	4.143±0.055	4.435±0.070	FLWO	Keplercam
4102.850	0.38	3.673±0.089	3.849±0.104	4.249±0.151	4.204±0.146	FLWO	Keplercam
4107.900	0.70	3.668±0.061	4.024±0.084	4.232±0.104	4.694±0.153	FLWO	Keplercam
4108.972	0.86	3.499±0.040	4.007±0.063	4.268±0.082	4.332±0.086	FLWO	Keplercam
4109.979	0.56	3.547±0.063	4.086±0.101	4.271±0.123	4.494±0.149	FLWO	Keplercam
4111.021	1.10	3.490±0.034	3.971±0.051	4.244±0.066	4.236±0.066	FLWO	Keplercam
4115.026	0.58	3.468±0.028	3.923±0.041	4.120±0.049	4.347±0.060	FLWO	Keplercam
4117.922	1.25	3.519±0.027	3.960±0.031	4.128±0.037	4.259±0.041	FLWO	Keplercam
4126.888	1.44	3.502±0.027	3.955±0.036	4.308±0.050	4.209±0.046	FLWO	Keplercam
4127.928	0.82	3.534±0.030	3.904±0.041	4.310±0.059	4.210±0.054	FLWO	Keplercam
4128.896	1.99	3.513±0.028	3.974±0.041	4.284±0.057	4.248±0.054	FLWO	Keplercam
4137.930	1.00	3.505±0.042	4.040±0.067	4.357±0.091	4.306±0.086	FLWO	Keplercam
4138.775	0.71	3.558±0.052	4.106±0.084	4.188±0.095	4.387±0.112	FLWO	Keplercam
4139.857	1.68	3.411±0.049	3.991±0.082	4.143±0.098	4.340±0.115	FLWO	Keplercam
4140.820	1.39	3.507±0.027	4.002±0.027	4.336±0.036	4.273±0.035	FLWO	Keplercam
4150.876	1.36	3.543±0.028	4.026±0.041	4.348±0.055	4.229±0.050	FLWO	Keplercam
4152.757	0.67	3.533±0.038	4.167±0.067	4.355±0.078	4.420±0.084	FLWO	Keplercam
4153.758	0.59	3.580±0.033	4.007±0.047	4.233±0.060	4.183±0.057	FLWO	Keplercam
4155.833	0.58	3.499±0.038	4.094±0.064	4.187±0.072	4.252±0.076	FLWO	Keplercam
4156.826	0.89	3.565±0.035	4.009±0.051	4.271±0.066	4.211±0.062	FLWO	Keplercam
4165.922	0.63	3.625±0.027	(4.455±0.027)	4.535±0.027	4.534±0.027	FLWO	Keplercam
4166.764	1.84	3.604±0.040	4.065±0.059	4.221±0.070	4.071±0.062	FLWO	Keplercam
4168.830	0.50	3.659±0.041	4.135±0.061	4.219±0.068	4.176±0.066	FLWO	Keplercam

TABLE 1—*Continued*

HJD	χ^2/N_{dof}	Image A	Image B	Image C	Image D	Observatory	Detector
4169.811	1.40	3.632±0.027	4.151±0.040	4.231±0.044	4.180±0.042	FLWO	Keplercam
4170.776	0.52	3.603±0.027	4.156±0.027	4.181±0.028	4.143±0.027	FLWO	Keplercam
4171.800	1.45	3.612±0.027	4.193±0.027	4.223±0.027	4.139±0.027	FLWO	Keplercam
4172.714	0.95	3.639±0.027	4.173±0.039	4.212±0.041	4.117±0.038	FLWO	Keplercam
4173.754	2.61	3.636±0.027	4.147±0.027	4.233±0.027	4.120±0.027	FLWO	Keplercam
4174.778	0.99	3.665±0.027	4.155±0.036	4.208±0.039	4.099±0.035	FLWO	Keplercam
4176.850	0.89	3.692±0.027	4.157±0.038	4.207±0.041	4.137±0.039	FLWO	Keplercam
4177.700	1.10	3.635±0.027	4.166±0.034	4.176±0.035	4.082±0.033	FLWO	Keplercam
4179.665	0.98	3.651±0.027	4.194±0.036	4.217±0.038	4.107±0.035	FLWO	Keplercam
4180.687	0.91	3.664±0.027	4.200±0.038	4.162±0.038	4.120±0.037	FLWO	Keplercam
4194.799	0.68	3.688±0.054	4.229±0.087	4.266±0.093	4.046±0.076	FLWO	Keplercam
4197.724	1.03	3.734±0.027	4.138±0.035	4.230±0.039	4.059±0.034	FLWO	Keplercam
4201.761	0.76	3.763±0.027	4.167±0.027	4.361±0.027	4.139±0.027	FLWO	Keplercam
4213.802	0.63	3.739±0.057	4.046±0.075	4.371±0.105	4.115±0.083	FLWO	Keplercam
4214.699	0.93	3.675±0.064	3.892±0.078	4.425±0.131	4.066±0.095	FLWO	Keplercam
4215.700	0.80	3.782±0.060	4.041±0.076	4.507±0.118	4.113±0.083	FLWO	Keplercam
4227.656	0.50	3.724±0.043	3.947±0.052	4.471±0.084	4.085±0.061	FLWO	Keplercam
4230.661	0.85	3.778±0.035	3.976±0.041	4.390±0.060	4.098±0.047	FLWO	Keplercam
4232.706	0.56	3.800±0.047	4.043±0.058	4.517±0.091	4.061±0.062	FLWO	Keplercam
4233.737	0.69	3.720±0.039	4.054±0.052	4.436±0.074	4.065±0.054	FLWO	Keplercam
4237.673	0.54	3.700±0.038	4.016±0.050	4.319±0.067	4.081±0.054	FLWO	Keplercam
4238.688	0.58	3.713±0.042	3.976±0.052	4.485±0.084	4.114±0.061	FLWO	Keplercam
4239.745	0.45	3.682±0.050	4.147±0.075	4.380±0.094	4.177±0.080	FLWO	Keplercam
4240.707	0.75	3.721±0.038	3.985±0.048	4.491±0.076	4.039±0.052	FLWO	Keplercam
4245.660	0.88	3.715±0.053	4.039±0.070	4.464±0.105	4.073±0.074	FLWO	Keplercam
4246.714	0.34	3.662±0.076	3.887±0.092	4.249±0.133	4.149±0.121	FLWO	Keplercam
4247.702	2.05	3.788±0.086	4.055±0.109	4.247±0.133	4.130±0.120	FLWO	Keplercam
4248.668	0.77	3.759±0.069	4.235±0.104	4.763±0.169	4.233±0.107	FLWO	Keplercam
4249.684	1.54	3.850±0.081	4.358±0.126	4.377±0.133	4.198±0.113	FLWO	Keplercam
4250.685	0.87	3.675±0.062	4.109±0.091	4.641±0.147	4.164±0.098	FLWO	Keplercam
4252.675	1.74	3.531±0.067	4.010±0.103	4.445±0.153	4.085±0.113	FLWO	Keplercam

TABLE 1—*Continued*

HJD	χ^2/N_{dof}	Image A	Image B	Image C	Image D	Observatory	Detector
4254.660	0.55	3.652±0.035	4.077±0.049	4.426±0.069	4.068±0.051	FLWO	Keplercam
4255.667	1.34	3.651±0.034	4.081±0.049	4.431±0.068	4.119±0.052	FLWO	Keplercam
4258.675	0.50	3.622±0.040	4.104±0.060	4.359±0.076	4.144±0.064	FLWO	Keplercam
4260.697	0.73	3.639±0.036	4.045±0.050	4.395±0.069	4.062±0.052	FLWO	Keplercam
4261.716	0.51	3.623±0.040	4.114±0.060	4.422±0.082	4.065±0.060	FLWO	Keplercam
4263.668	0.48	3.651±0.050	4.231±0.083	4.314±0.092	4.117±0.077	FLWO	Keplercam
4264.654	0.69	3.615±0.046	4.098±0.069	4.467±0.096	4.032±0.067	FLWO	Keplercam
4265.685	0.48	3.693±0.046	4.141±0.068	4.301±0.081	4.114±0.069	FLWO	Keplercam
4266.700	0.73	3.531±0.068	4.243±0.129	4.148±0.124	4.253±0.135	FLWO	Keplercam
4269.687	1.27	3.704±0.083	4.117±0.120	4.426±0.159	3.972±0.111	FLWO	Keplercam
4271.674	0.44	3.742±0.077	3.960±0.093	4.317±0.133	4.037±0.104	FLWO	Keplercam
4276.677	0.36	3.720±0.077	4.101±0.107	4.360±0.140	4.122±0.113	FLWO	Keplercam
4277.649	0.25	3.695±0.167	3.986±0.213	4.195±0.266	4.277±0.282	FLWO	Keplercam
4278.668	0.32	3.615±0.079	4.099±0.121	4.576±0.190	4.002±0.116	FLWO	Keplercam

NOTE.—The Heliocentric Julian Days (HJD) column gives the date of the observation relative to HJD=2450000. The χ^2/N_{dof} column indicates how well our photometric model fit the imaging data. When $\chi^2 > N_{dof}$ we rescale the photometric errors presented in this Table by $(\chi^2/N_{dof})^{1/2}$ before carrying out the time delay analysis to reduce the weight of images that were fit poorly. The image magnitudes are relative to the comparison stars (see text). The magnitudes enclosed in parentheses are not used in the time delay estimates.